Photoelectron spectrometer for liquid and gas-phase attosecond spectroscopy with field-free and magnetic bottle operation modes

Inga Jordan, Arohi Jain, Thomas Gaumnitz, Jun Ma, and Hans Jakob Wörner

Citation: Review of Scientific Instruments **89**, 053103 (2018); doi: 10.1063/1.5011657
View online: https://doi.org/10.1063/1.5011657
View Table of Contents: http://aip.scitation.org/toc/rsi/89/5
Published by the American Institute of Physics

Photoelectron spectrometer for liquid and gas-phase attosecond spectroscopy with field-free and magnetic bottle operation modes

Inga Jordan, Arohi Jain, Thomas Gaumnitz, Jun Ma, and Hans Jakob Wörner[a)]
Laboratory of Physical Chemistry, ETH Zurich, Vladimir-Prelog-Weg 2, 8093 Zurich, Switzerland

(Received 1 November 2017; accepted 15 April 2018; published online 3 May 2018)

A compact time-of-flight spectrometer for applications in attosecond spectroscopy in the liquid and gas phases is presented. It allows for altering the collection efficiency by transitioning between field-free and magnetic-bottle operation modes. High energy resolution ($\Delta E/E = 0.03$ for kinetic energies >20 eV) is achieved despite the short flight-tube length through a homogeneous deceleration potential at the beginning of the flight tube. A closing mechanism allows isolating the vacuum system of the flight tube from the interaction region in order to efficiently perform liquid-microjet experiments. The capabilities of the instrument are demonstrated through photoelectron spectra from multiphoton ionization of argon and xenon, as well as photoelectron spectra of liquid and gaseous water generated by an attosecond pulse train. *Published by AIP Publishing.* https://doi.org/10.1063/1.5011657

I. INTRODUCTION

Following electron dynamics in real time requires the involvement of attosecond techniques[1–5] which rely on the detection of either high-harmonic emission or absorption or electrons and ions generated using high-harmonic radiation. This makes a photoelectron spectrometer an important prerequisite for several attosecond experiments and calls for compact and versatile instruments with high energy resolution.

Additionally, being the most common environment for chemical reactions, biological processes, and catalytic cycles, the liquid phase is of particular interest when fundamental and applied sciences are to be bridged. The liquid microjet technique[6,7] made the liquid phase compatible with the high-vacuum requirements for extreme ultraviolet (XUV) radiation and photoelectron spectroscopy and thus provided the prerequisite for extending attosecond science to the liquid phase.[8] This opens the path for the investigation of ionization, thermalization, and ultrafast motion of photoelectrons generated in a liquid environment. Various liquid-microjet photoelectron spectrometers have been described,[9–11] and several experiments with picosecond to femtosecond temporal resolution have already been reported.[12–18] However, attosecond time-resolved measurements on liquid samples have not been reported yet.

Two of the most common attosecond techniques based on the detection of photoelectrons are RABBIT (reconstruction of attosecond beating by interference of two-photon transitions) and the attosecond-streaking technique.[1,19–22] These two methods have been used to measure attosecond photoionization delays of atoms,[23–25] molecules,[26] and solids.[27–29]

In attosecond streaking, the analysis is usually restricted to electrons collected from a small solid angle and thus requires a field-free operation of the photoelectron spectrometer. Also, any sort of angular-resolved measurement limits the collection angle of the spectrometer. A velocity-map-imaging spectrometer would allow for collection angles of 2π sr; however, the inhomogeneous electric-field distribution around the liquid jet may prevent the inversion of velocity-image data.

RABBIT benefits from highly resolved photoelectron spectra which require narrow-bandwidth high-harmonic radiation as well as a spectrometer with the highest possible energy resolution. High count rates ensure short acquisition times and the collection of a sufficiently high number of spectra to ensure reproducibility and an error estimation of the obtained attosecond delays. However, space-charge effects have to be avoided, and high count rates can therefore only be achieved by increasing the collection efficiency of the spectrometer, for example, in a magnetic bottle design.[8,30]

These considerations demonstrate the necessity of a high-resolution photoelectron spectrometer capable of adjusting the collection angle to suit both purposes, attosecond streaking and RABBIT. Also, the spectrometer should feature liquid microjets as a possible target. In this article, we demonstrate the realization of such a photoelectron time-of-flight spectrometer where switching between field-free and magnetic-bottle operational modes is based on placing a permanent magnet at the entrance aperture of the flight tube. An intermediate regime between field-free and magnetic-bottle configuration can be realized by using a homogeneous guiding magnetic field in the drift region, which allows increasing the collection angle by a factor of 10-20 depending on the strength of the homogeneous magnetic guiding field in the drift region.

II. INSTRUMENT DESIGN

The design of the spectrometer was guided by the following aspects. First, as the collection angle is supposed to be flexible, a combination of field-free and magnetic-bottle modes of operation was chosen as a basis for the design. The spectrometer is equipped with a solenoid inside the flight tube, and a permanent magnet (SmCo, double stack of 25 × 15 cylinders, 1 T remanence field strength, and tapered soft iron tip with flattened top) can optionally be introduced in the interaction region. Second, for the high-resolution requirements, the

a)Electronic mail: hwoerner@ethz.ch

length of the drift tube should be maximized; however, electron losses in the field-free operational mode due to stray electric or magnetic fields become more probable, and also the collection angle becomes too small for reasonable field-free acquisition times. For these reasons, the distance between the points of ionization and detection was limited to 0.5 m, which still gives an acceptance angle of 0.0023 sr in field-free mode (detection area of 27 mm), and electroformed retardation meshes (copper wires, 117.6 lines per inch, 88.6% transmission, and rectangular aperture) were implemented between the skimmer and the beginning of the drift tube. Thus, fast electrons can be retarded to low kinetic energies, where the resolution is higher. Third, since the interaction chamber is supposed to be compatible with gas and liquid targets, liquid nitrogen cold traps are unavoidable in the interaction region. We found that the pumping speed of the turbomolecular pumps (TMP) is less critical for the final pressure in the interaction region; however, efficient cooling is sufficient to reach the required low pressures once the interaction chamber volume has been pumped. The liquid nitrogen cold traps therefore enhance the pumping speed by several orders of magnitude for all gaseous components subject to deposition at 77 K. However, a small turbo pump is still required to remove residual evaporating gas not captured by the cold trap and to isolate interaction chamber pressures of less than 1×10^{-4} mbar against prevacuum pressures.

Finally, performing attosecond experiments requires an attosecond delay line in order to control the delay between ionizing and assisting pulses. Typically, this is realized through a beamline[31–33] or by a piezo-based mirror delay-stage at normal incidence.[27,34] The former requires vibrationally decoupled accurate positioning of the spectrometer entrance port with respect to the beamline exit port, whereas for the latter a mirror delay stage can be attached to the spectrometer exit port. The design presented here allows the realization of both options using a home-built spectrometer frame allowing three-dimensional positioning with 50 μm precision and an additional vacuum chamber that contains the mirror delay-stage. The spectrum of the XUV radiation can be easily monitored by attaching a slit-grating photon spectrometer to one of the various ports of the experimental chamber.

The resulting design is presented in Fig. 1, where the interaction chamber is shown from the side with a vertical cut through the interaction region. The laser propagation is perpendicular to that plane. The interaction chamber is separated from the flight tube by using a gold-coated skimmer with an exchangeable aperture of 0.5 mm. The flight-tube is equipped with a one-layered solenoid (0.96 m^2 wire cross-sectional area, 0.25 mm insulation thickness, wiring slope 2.5 mm, and number of turns ~200) and a μ-metal tube (95 mm inner diameter and 3 mm thickness) and pumped directly behind the skimmer entrance by using a TMP. Holes in the μ-metal and solenoid tubing ensure sufficient pumping to reach pressures below 10^{-5} mbar in the flight tube. Depending on the gas load in the interaction chamber, a second TMP can be installed at the end of the flight tube. The high-vacuum flight tube can be sealed against the interaction chamber by pressing a viton-bonded cap against the skimmer using a home-built manipulator. This allows for venting and pumping of the interaction chamber without affecting the high-vacuum in the flight-tube region.

Electrons are detected by using a commercially available pair of microchannel plates in chevron configuration (27 mm active area and impedance-matched anode) at the end of the flight tube. The MCP response function is Gaussian-shaped with a full width at half maximum (FWHM) of less than 1 ns, which ensures that the photoelectron spectra are not limited by the detector response. The specific anode design accounts for the flattening of the overshoot and ringing behavior of the MCP response. However, it can be further improved by adjusting the impedance of the high-voltage supply leads. These measures ensure that no artefacts from the MCP response become imprinted in the photoelectron spectra.

A digitizer card (Agilent U1071A 8-bit High-Speed PCI Digitizer, 2 GS/s real-time sampling rate) is used to process the anode signal on a single-shot basis. The smallest time bin on the time-of-flight axis supported by this card is 0.5 ns. The digitized single-shot spectrum can be either stored for averaging or fed into a time-to-digital conversion (tdc) procedure. The latter is based on assigning a value of 1 to each time bin, where an electron was detected, and setting all others to zero. Averaging must only be performed if the post-pulse behavior is sufficiently flat. The tdc mode on the other hand can handle ringing as long as the ringing amplitude is sufficiently small compared to the main peak height. In both cases, the FWHM of the MCP response has to be smaller than the size of the time bins; otherwise, an additional broadening is expected upon averaging or a peak-finding algorithm has to be implemented when using the tdc acquisition mode.

In the field-free operation mode, any electric or magnetic stray fields can have an adverse effect on the photoelectron spectra, and for this reason μ-metal shielding of the interaction region and the flight tube are essential. The shielding for the interaction region can be removed when inserting the permanent magnet for magnetic-bottle operation mode in order to gain better visibility on the interaction region. It is also possible to remove the permanent magnet and to just use the solenoid in order to guide electrons which have already entered the flight tube. The retardation meshes are placed such that the retardation is only applied after the momenta of the electrons have been parallelized.

A. Targets

The liquid microjet setup has been described in detail elsewhere.[8] Briefly, using a high-pressure liquid chromatography (HPLC) pump, the solution to be studied is pumped from a reservoir through 1/16″ polyether ether ketone (PEEK) tubing and is injected into the interaction chamber through a nozzle. Quartz nozzles for liquid jet applications in a vacuum are commercially available in various sizes. Nozzle diameters between 15 and 50 μm are typically used in our setup. The jet can be positioned with 1 nm resolution by using xyz positioners (SmarAct GmbH, closed-loop and repeatability ±30 nm) which are mounted on a holder on the bottom flange of the interaction chamber.[35] The liquid filament streams into a stainless steel catcher which is cooled on the atmospheric side with

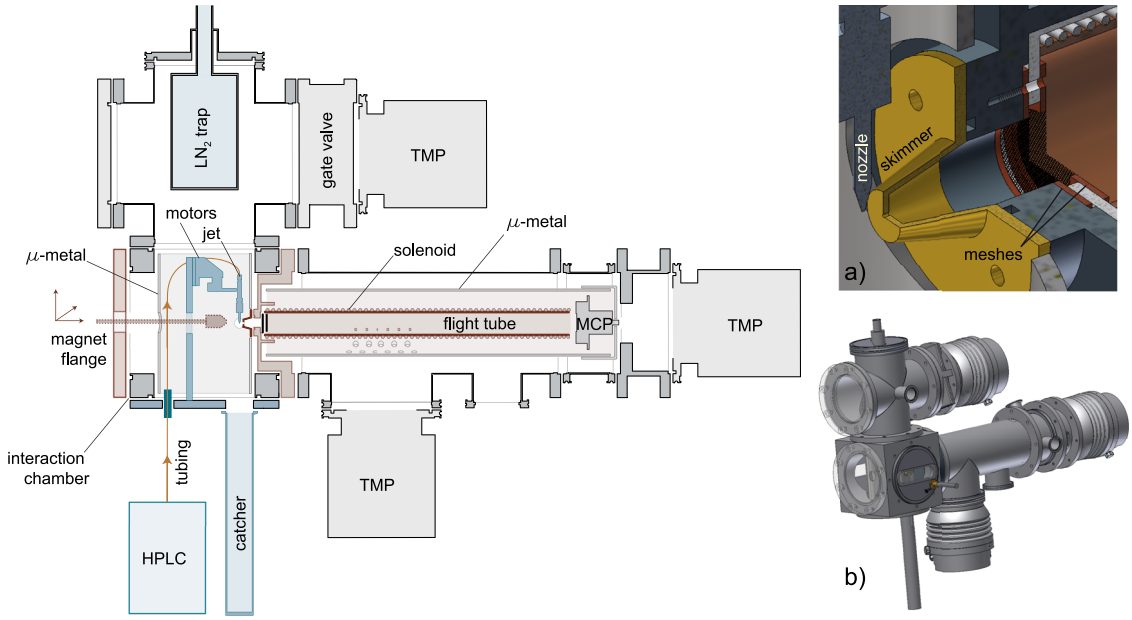

FIG. 1. Schematic overview of the time-of-flight spectrometer with optional magnetic-bottle operation. Liquid jet parts are shown in blue. The inset (a) shows an enlargement of the interaction region and the two retardation meshes. The inset (b) shows the complete layout of the spectrometer as a three-dimensional rendering.

liquid nitrogen and freezes the solution as it hits the catcher walls. Depending on the vapor pressure of the liquid, the microjet has to be started under atmospheric pressure and only afterwards the interaction region can be pumped down. This is particularly the case for liquid water. Any interruption of the liquid flow under vacuum leads to an immediate freezing of the liquid and requires venting the interaction chamber for restarting the microjet. However, the pressure must not necessarily increase to 1 atm, as the jet might restart once the frozen part has melted.

For both calibration and comparison purposes, recording gas-phase data greatly facilitates the analysis of the liquid-phase photoelectron spectra. Therefore, a combined nozzle holder for the liquid microjet and a gas nozzle has been designed and is shown in Fig. 2. Using the positioning motors, either the gas or the liquid can be placed in the interaction region. In order to remain in a sufficiently low pressure regime with both nozzles operating simultaneously, a continuous gas nozzle with a tapered orifice with diameters between 10 μm and 50 μm has been used when operating the liquid and gas jets simultaneously.

B. Radiation sources

The output of an amplified Ti:Sa femtosecond laser centered at 800 nm is used either for above threshold ionization (ATI)[36,37] by directly focusing the near-infrared laser pulses onto the target or for high-harmonic generation[38,39] in a gas target. In the latter case, the fundamental infrared beam is focused onto a high-density noble gas target (10-500 mbar depending on the gas) housed in a differentially pumped vacuum chamber system. High-order harmonic radiation is generated in the focal region and propagates collinearly with the residual fundamental beam into an intermediate vacuum chamber for beam modifications (filtering of harmonic orders, removal of residual infrared radiation, and attenuation using an aperture) before passing the interaction region and being refocused onto the target.

Characteristics of the XUV photon spectrometer have been published elsewhere.[8] Briefly, XUV radiation transmitted through the interaction region passes an adjustable slit and is afterwards dispersed by using a grating with 1200 lines/mm onto a MCP with a phosphor screen. Harmonic energies and widths can then be extracted from the diffraction image.

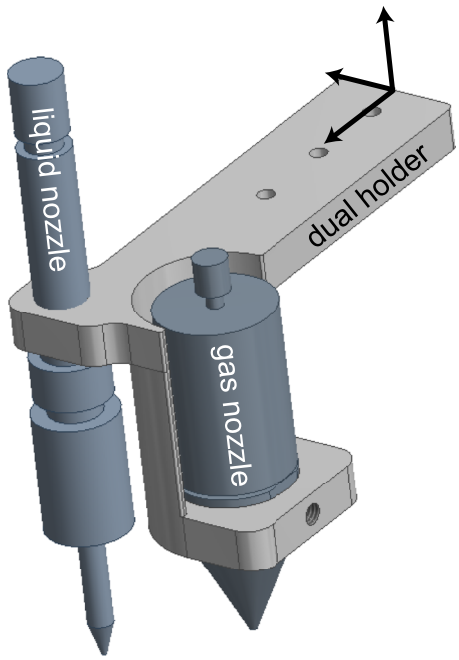

FIG. 2. Combined holder for liquid and gas nozzles.

III. INSTRUMENT PERFORMANCE

For the characterization of the instrument, the above-threshold ionization peaks of xenon have been used. Electrons generated in this way cover a broad range of kinetic energies, all peaks being spaced by the photon energy of 1.55 eV. The influence of retardation and the comparison between field-free and magnetic-bottle operation modes can thus be conducted with ATI spectra. The ATI spectra presented in this article were generated under identical conditions except for the laser intensity, which was adjusted using a continuous neutral density filter in order to cover the different collection efficiencies between the field-free and magnetic-bottle operation modes. In addition, the acquisition times were also adjusted. The f-number for our settings was approximately 40. Similarly, the gas pressures were adjusted as well.

The effect of deceleration on the peak width, however, cannot be seen in ATI spectra since in this case the width of the peaks is dominated by the ATI process itself and not by the spectrometer. Thus, no gain of resolution due to retardation is observed when analyzing ATI spectra as a function of the retardation voltage. In order to characterize the effect of the retardation voltage on the photoelectron signal, high-harmonic radiation has been used. The bandwidth of the harmonic orders used here (57-61) is typically around 0.3 eV and is influenced by the details of the experimental conditions, such as the daily alignment, pulse-compression settings, gas-cell pressure, etc.

A. Calibration and conversion

A typical ATI spectrum of Xe recorded with 800 nm radiation in the field-free operational mode is presented in Fig. 3(a). Line shapes are generally very well reproduced using Gaussian functions. For the low-kinetic-energy bands, however, a more complicated peak shape is observed. This finding is assigned to the spin-orbit splitting (1.306 eV[40]) of the ^{2}P-ground state of Xe^+ which lies close to the photon energy of 1.55 eV such that the two ATI combs associated with each spin-orbit component are separated by 0.24 eV and thus can still be partially resolved.[41]

Kinetic energies for each ATI peak have been calculated based on the number (n) of involved photons and the binding energy of xenon and plotted against the corresponding flight times extracted from the Gaussian fits (orange filled circles). A conversion function $[E_{\mathrm{kin}} = \frac{m}{2}\left(\frac{s}{t-t_0}\right)^2 + E_0$, where t is the flight time and m is the electron mass] has been fitted to this data set (orange line) in order to extract the fit parameters s, the flight path length, t_0, the temporal offset between the data acquisition starting point and the actual instant of ionization, and E_0, an energy offset. The latter parameter also reflects the intensity-dependent spectral shift occurring in ATI spectra. Using these parameters, the time-of-flight axis can be converted into a kinetic-energy axis and interpolated onto an equidistant kinetic-energy grid. The spectral amplitudes are then Jacobi-corrected in order to preserve the peak integrals after conversion. A converted ATI spectrum is presented in Fig. 3(b). The position of the ATI peaks according to the formula $E_{\mathrm{kin}} = nh\nu - I_p - U_p$ is indicated, where n is the number of photons with energy $h\nu$, I_p is the ionization potential, and U_p is the ponderomotive potential, which in our case amounts to approximately 6 eV. The energy offset has not been corrected for ATI-spectra since it depends on the intensity of the infrared radiation. All measurement series have been recorded under the same ionization conditions; thus, the energy offset is identical for all spectra within the same series, e.g., coil current, retardation potential, etc.

B. Retardation and resolution

Converted, Jacobi-corrected, and interpolated ATI spectra generated by ionizing Xe with a 25-fs laser pulse centered at 800 nm with 75 μJ pulse energy and recorded at different retardation voltages are shown in Fig. 4(a). Peak positions and integrals as a function of the retardation voltage are presented in Figs. 4(b) and 4(c). Due to the more complicated line shapes at the low-kinetic-energy side of the spectrum, a single Gaussian fit to each component was not possible; at the same time, a double Gaussian fit at the high-kinetic energy side was not feasible either. Since the ATI peaks are still nearly baseline-resolved, their position has been determined by the center-of-energy of the individual peak. The peak shifts follow the applied retardation potential linearly allowing the shift of any desired part of the photoelectron spectrum to the low-kinetic energy side. Recording several photoelectron spectra consecutively at different retardation voltages allows generating a high-resolution photoelectron spectrum despite the short flight-tube length.

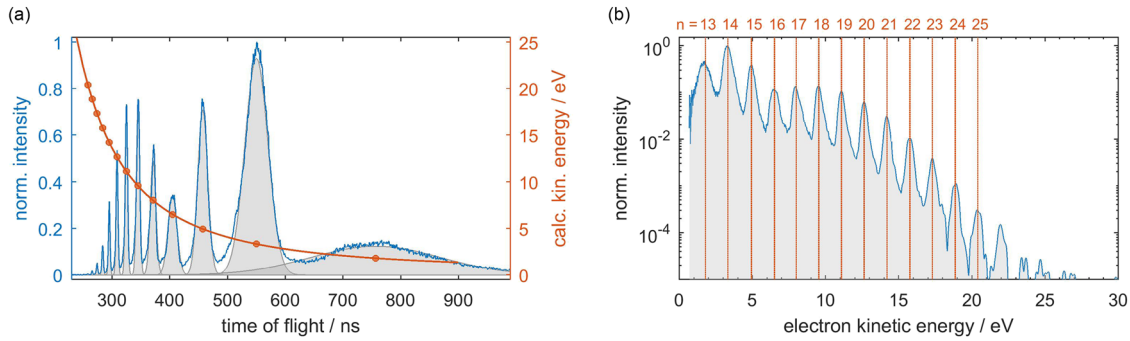

FIG. 3. (a) ATI time-of-flight spectrum generated by above-threshold ionization (ATI) of Xe with 800 nm pulses with ~25 fs pulse duration and 70 μJ pulse energy in the field-free operation mode. The calibration curve is shown as the orange solid line, and circles represent the expected kinetic energies of the extracted flight times. Gaussian fits are represented by gray filled curves. (b) Jacobi-corrected, interpolated, and energy-converted Xe ATI spectrum shown in (a). Vertical lines are spaced by 1.55 eV and correspond to the kinetic energy of electrons created by ionization of Xe to the $^2P_{3/2}$ ground state of Xe^+ by n 800 nm photons.

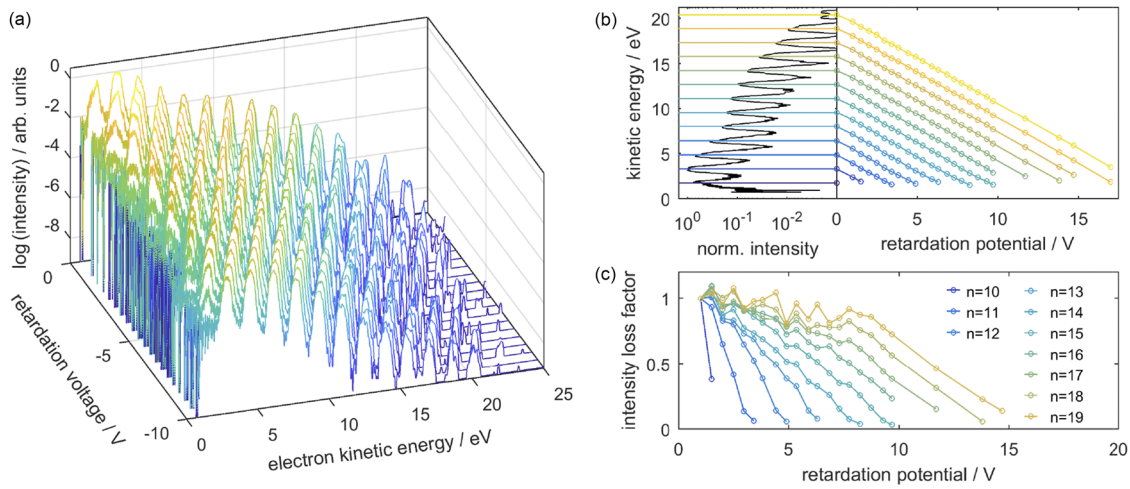

FIG. 4. ATI spectra generated by multi-photon ionization of xenon with a 25-fs laser pulse centered at 800 nm with 75 μJ pulse energy as a function of the retardation potential. (a) Individual photoelectron spectra. (b) Extracted center-of-energy of each ATI peak as a function of the retardation potential. (c) Relative peak integrals as a function of the retardation voltage.

However, the peak integrals were found to decrease with increasing retardation potential, which is attributed to electron deflection and subsequent loss caused by the electric-field inhomogeneities in close proximity to the mesh grid lines. The electron loss is more pronounced for low-kinetic-energy electrons. For this particular design, retardation to a final kinetic energy below 2 eV leads to a signal intensity loss of about 50%.

In order to characterize the resolution of the spectrometer as a function of the retardation voltage, odd harmonic orders 55-61 reflected under normal incidence by using a multi-layer-coated XUV focusing mirror were used to ionize argon. Spectra were recorded at different retardation voltages. A coil current of 0.5 A was used to guide electrons which entered the flight tube (no permanent magnet). Photoelectron spectra generated by ionization from the outermost *p*- and *s*-shells of argon are shown as an example for three different retardation voltages in Fig. 5(a). The results of the analysis of the peak width as a function of the retardation voltage are summarized in Fig. 5(b).

The peak width ΔE decreases linearly with the applied voltage. Averaging the $\Delta E/E_{\mathrm{kin}}$ values for all measurement points above 20 eV gives a relative spectrometer energy resolution of 0.03. The evolution of photoelectron spectra as a function of the retardation potential shows impressively the transition from extensive peak overlap to baseline resolution. The only drawback of the retardation principle as realized here is the loss of electron counts and thus the longer integration times. As demonstrated in Sec. III C, electron losses can be compensated by exploiting a homogeneous magnetic guiding field in the flight tube.

C. Coil influence

The influence of the coil current on the ATI spectrum is presented in Fig. 6. Here, the spectrometer was operated without a permanent magnet, and therefore, all electrons were guided along the homogeneous magnetic field lines toward the detector once they entered the flight tube. The signal is amplified nearly homogeneously above 4 eV kinetic energy, i.e., for a number (n) of absorbed photons of 15 and higher. The larger amplification factors for slow electrons ($n = 13$) are attributed to the fact that the latter are collected more efficiently by the guiding magnetic field compared to the faster electrons.

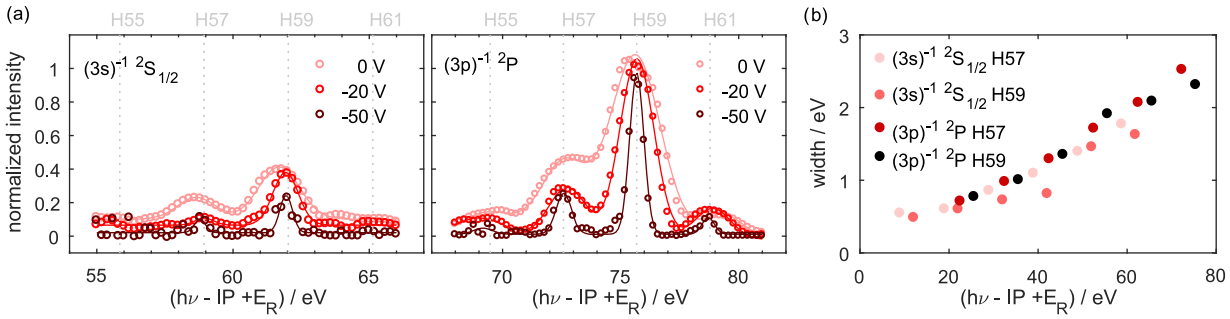

FIG. 5. (a) Photoelectron spectrum of argon generated with odd harmonic orders 55-61 (H55, H57, H59, and H61) at three different retardation voltages, E_R. The x-axis is given as the difference between the photon energy, $h\nu$, minus the ionization potential I_P plus the retardation voltage. Solid lines represent a fit using the sum of four Gaussian functions representing the photoelectrons generated with each harmonic orders (55, 57, 59, and 61) reflected by the XUV mirror. The peak is associated with ionization into the ^2P spin-orbit split final states; however, the splitting is smaller than the energy resolution at all retardation voltages. (b) Peak width as a function of the kinetic energy after retardation, as determined from the retardation measurement series. The count rates in these data sets ranged from 0.08 to 1.0 electrons/laser shot.

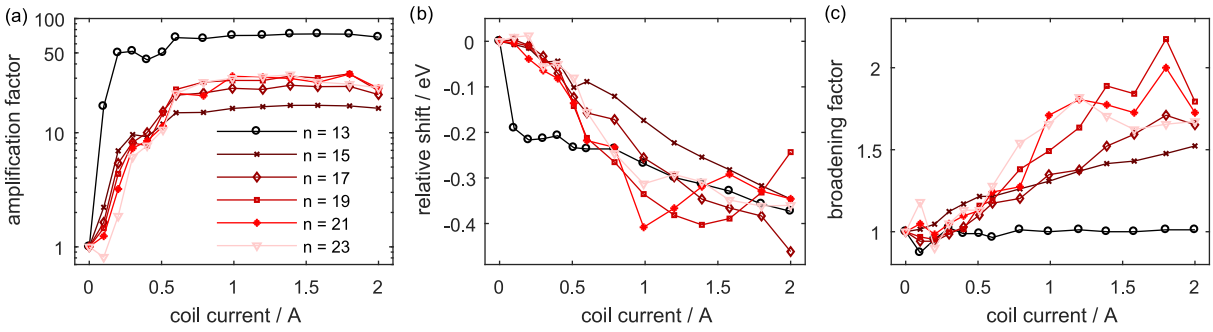

FIG. 6. Influence of the coil current on the ATI spectrum of xenon generated with 800 nm pulses and 85 μJ pulse energy in the absence of the permanent magnet. (a) Signal amplification as a function of the coil current. (b) Relative shift of each peak as a function of the coil current. (c) Broadening of ATI peaks as a function of the coil current. The integer numbers n given in the legend refer to the number of photons corresponding to each ATI peak in the spectrum.

The overall amplification increases until a current of 0.4 A is reached and then levels off to an amplification factor of at least 10. The gas pressure was reduced compared to Figs. 3 and 4 in order to avoid the saturation of the detector when enhancing the electron signal intensity. Additionally, the laser intensity was increased in order to generate high ATI orders and thereby to cover a broad range of kinetic energies.

However, both peak positions and peak widths are affected by the presence of the magnetic field in the drift region. The photoelectron peaks are shifted toward lower kinetic energies as a function of an increasing coil current [Fig. 6(b)]. The width of the ATI peaks increases as a function of the coil current, which is more pronounced for higher kinetic-energy electrons [Fig. 6(c)]. Both effects can be understood in terms of the redirection of electrons inside the flight tube. Only the velocity component parallel to the magnetic field lines influences the measured flight time, whereas the perpendicular component causes a helical motion due to the Lorentz force. Electrons with emission angles larger than the acceptance angle permitted by the field-free design can therefore be collected, but they arrive later at the detector than those emitted with small angles. This effect shifts the maximum of the peak to longer time of flights, i.e., lower apparent kinetic energies, and causes a peak broadening.

D. Magnetic bottle

Inserting the permanent magnet into the interaction region and applying a current to the solenoid in the flight tube allows collecting electrons in a magnetic-bottle configuration. In general, the signal intensity is strongly enhanced by the mere presence of the permanent magnet in the interaction region and increases further when increasing the coil current. However the peak width is also broadened by the presence of the permanent magnet as compared to the field-free operational mode. The intensity of the infrared radiation had to be reduced in order to avoid detector saturation or even damage. For this reason, the intensity was kept relatively low such that the highest-order observed ATI peak corresponded to $n = 19$ photons.

The ATI spectra of Xe recorded in the magnetic-bottle configuration were evaluated as a function of the solenoid current (Fig. 7), similar to what has already been presented for the field-free operational mode in Sec. III C. The amplification is nearly homogeneous over the entire spectral range covered by the ATI peaks here. The relative shift remains at 0.1 eV above a coil current of 0.5 A, and the broadening is negligible. This behavior was confirmed for several retardation voltages. However, electron losses at higher retardation voltages are also observed.

IV. LIQUID- AND GAS-PHASE WATER

In order to illustrate representative spectra from the liquid microjet source, we have recorded liquid-water photoelectron spectra using a high-harmonic source. Odd harmonic orders 11-15 were transmitted through a 0.2 μm-thick tin filter. NaCl with a concentration of 0.05 mol/l was added to minimize the

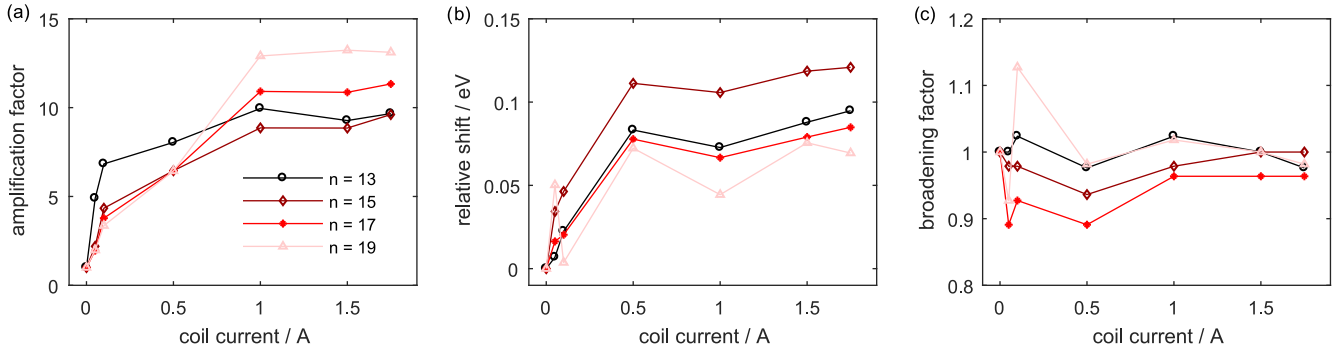

FIG. 7. Influence of the coil current on the ATI spectrum of xenon generated with 800 nm pulses and 23 μJ pulse energy in the magnetic-bottle operation mode (using the permanent magnet). (a) Signal amplification as a function of the coil current. (b) Relative shift of each peak as a function of the coil current. (c) Broadening of ATI peaks as a function of the coil current. The integer numbers n given in the legend refer to the number of photons corresponding to each ATI peak in the spectrum.

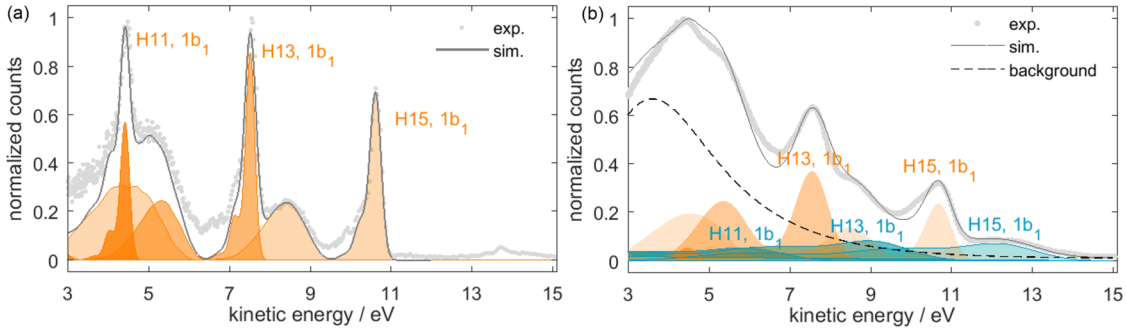

FIG. 8. (a) Gas-phase water photoelectron spectrum generated with harmonic radiation containing orders 11-15 of the 800-nm fundamental. (b) Liquid-phase water photoelectron spectrum generated with harmonic orders 11-15. Gas-phase contributions are in orange, whereas liquid-phase contributions are in blue. The gas-phase contribution arises from water molecules evaporating from the liquid jet. The text labels refer to the harmonic order and the orbital/band that was ionized. The spectra in both panels were recorded in the field-free configuration.

effects of electrokinetic charging. Photoelectrons from the gas phase surrounding the liquid jet due to evaporation were collected as well. For better deconvolution, it is beneficial to also record the pure gas-phase spectra. Attention has to be paid to the streaming potential of the liquid jet which affects the width and position of the gas-phase signal.[6,7,15,42–44] The experimental data are shown together with a simulation in Fig. 8. The count rates amounted to 0.6-0.7 and 5-7 electrons/laser shot in Figs. 8(a) and 8(b), respectively. In both cases, the calibration of the photoelectron spectra were carried out on the basis of the same photoelectron spectra of gaseous argon, ionized with the same harmonic orders (11-15). Since the kinetic energies of the photoelectron bands from gaseous water agree between the two measurements, we can exclude a space-charge induced shift of these bands within the accuracy of our calibration (0.1-0.2 eV).

The simulation is based on the superposition of spectra generated with binding energies and widths of the photoelectron bands taken from the literature.[42,45,46] The spectra were further broadened in order to account for the spectrometer function, as well as the influences of a residual streaming potential and a possible vacuum-level offset on the gas-phase signal. Both of these effects were indeed shown to broaden the gas-phase photoelectron peaks because of the inhomogeneous electric-field distribution that they create.[42,43] The agreement between the experimental and the simulated spectra is generally very good. Small deviations are observed in between the strongest bands. The large contributions of the gas-phase signals relative to the liquid-phase signals are explained by the fact that the high-harmonic radiation was not refocused in these experiments such that the XUV spot size amounted to ~0.5 mm on the liquid jet.

V. CONCLUSIONS

We have demonstrated that the combination of a field-free time-of-flight spectrometer with a solenoid and an optional permanent magnet allows for a straightforward transition between field-free and magnetic-bottle operation mode, thereby altering the collection efficiency. Using retardation meshes, fast electrons can be decelerated to low kinetic energies and thus a better spectral resolution can be achieved. The associated electron loss at very low kinetic energies after retardation can be partially compensated by the improved collection efficiency originating from the guiding magnetic field generated by the solenoid in the drift region. The compact design and the flexibility in terms of the collection efficiency allow performing RABBIT and streaking experiments with optimized resolution and acquisition times. This design is compatible with both, gas and liquid microjet targets. This photoelectron spectrometer is therefore ideally suitable for performing attosecond time-resolved measurements on gases and liquids, using either the RABBIT or attosecond-streaking techniques.

ACKNOWLEDGMENTS

The authors thank A. Laso for the design and construction of the spectrometer frame and A. Schneider for assistance with electronics. The authors greatly appreciate discussions with M. Huppert and B. Niraghatam Ram. This work was supported by the Swiss National Science Foundation under Project No. 200021E-162822.

[1] M. Hentschel, R. Kienberger, C. Spielmann, G. A. Reider, N. Milosevic, T. Brabec, P. Corkum, U. Heinzmann, M. Drescher, and F. Krausz, Nature **414**, 509 (2001).
[2] F. Krausz and M. Ivanov, Rev. Mod. Phys. **81**, 163 (2009).
[3] H. J. Wörner and P. B. Corkum, "Attosecond spectroscopy," in *Handbook of High Resolution Spectroscopy* (John Wiley and Sons, Ltd., Chichester, 2011).
[4] Z. Chang, *Fundamentals of Attosecond Optics* (CRC Press, 2011).
[5] F. Calegari, G. Sansone, S. Stagira, C. Vozzi, and M. Nisoli, J. Phys. B: At., Mol. Opt. Phys. **49**, 062001 (2016).
[6] M. Faubel, B. Steiner, and J. P. Toennies, J. Chem. Phys. **106**, 9013 (1997).
[7] B. Winter and M. Faubel, Chem. Rev. **106**, 1176 (2006).
[8] I. Jordan, M. Huppert, M. A. Brown, J. A. van Bokhoven, and H. J. Wörner, Rev. Sci. Instrum. **86**, 123905 (2015).
[9] A. T. Shreve, T. A. Yen, and D. M. Neumark, Chem. Phys. Lett. **493**, 216 (2010).
[10] A. Kothe, J. Metje, M. Wilke, A. Moguilevski, N. Engel, R. Al-Obaidi, C. Richter, R. Golnak, I. Y. Kiyan, and E. F. Aziz, Rev. Sci. Instrum. **84**, 023106 (2013).
[11] C. A. Arrell, J. Ojeda, M. Sabbar, W. A. Okell, T. Witting, T. Siegel, Z. Diveki, S. Hutchinson, L. Gallmann, U. Keller *et al.*, Rev. Sci. Instrum. **85**, 103117 (2014).
[12] K. R. Siefermann, Y. Liu, E. Lugovoy, O. Link, M. Faubel, U. Buck, B. Winter, and B. Abel, Nat. Chem. **2**, 274 (2010).
[13] M. H. Elkins, H. L. Williams, A. T. Shreve, and D. M. Neumark, Science **342**, 1496 (2013).
[14] F. Buchner, A. Nakayama, S. Yamazaki, H.-H. Ritze, and A. Lübcke, J. Am. Chem. Soc. **137**, 2931 (2015).

[15]F. Buchner, A. Lübcke, N. Heine, and T. Schultz, Rev. Sci. Instrum. **81**, 113107 (2010).
[16]O. Link, E. Lugovoy, K. Siefermann, Y. Liu, M. Faubel, and B. Abel, Appl. Phys. A **96**, 117 (2009).
[17]Y. Tang, Y.-i. Suzuki, H. Shen, K. Sekiguchi, N. Kurahashi, K. Nishizawa, P. Zuo, and T. Suzuki, Chem. Phys. Lett. **494**, 111 (2010).
[18]Y.-I. Suzuki, H. Shen, Y. Tang, N. Kurahashi, K. Sekiguchi, T. Mizuno, and T. Suzuki, Chem. Sci. **2**, 1094 (2011).
[19]P. M. Paul, E. S. Toma, P. Breger, G. Mullot, F. Auge, P. Balcou, H. G. Muller, and P. Agostini, Science **292**, 1689 (2001).
[20]H. G. Muller, Appl. Phys. B **74**, s17 (2002).
[21]J. Itatani, F. Quéré, G. L. Yudin, M. Y. Ivanov, F. Krausz, and P. B. Corkum, Phys. Rev. Lett. **88**, 173903 (2002).
[22]M. Kitzler, N. Milosevic, A. Scrinzi, F. Krausz, and T. Brabec, Phys. Rev. Lett. **88**, 173904 (2002).
[23]M. Schultze, K. Ramasesha, C. D. Pemmaraju, S. A. Sato, D. Whitmore, A. Gandman, J. S. Prell, L. J. Borja, D. Prendergast, K. Yabana *et al.*, Science **346**, 1348 (2014).
[24]K. Klünder, J. M. Dahlström, M. Gisselbrecht, T. Fordell, M. Swoboda, D. Guénot, P. Johnsson, J. Caillat, J. Mauritsson, A. Maquet *et al.*, Phys. Rev. Lett. **106**, 143002 (2011).
[25]I. Jordan, M. Huppert, S. Pabst, A. S. Kheifets, D. Baykusheva, and H. J. Wörner, Phys. Rev. A **95**, 013404 (2017).
[26]M. Huppert, I. Jordan, D. Baykusheva, A. von Conta, and H. J. Wörner, Phys. Rev. Lett. **117**, 093001 (2016).
[27]A. L. Cavalieri, N. Müller, T. Uphues, V. S. Yakovlev, A. Baltuska, B. Horvath, B. Schmidt, L. Blümel, R. Holzwarth, S. Hendel *et al.*, Nature **449**, 1029 (2007).
[28]S. Neppl, R. Ernstorfer, A. L. Cavalieri, C. Lemell, G. Wachter, E. Magerl, E. M. Bothschafter, M. Jobst, M. Hofstetter, U. Kleineberg *et al.*, Nature **517**, 342 (2015).
[29]R. Locher, L. Castiglioni, M. Lucchini, M. Greif, L. Gallmann, J. Osterwalder, M. Hengsberger, and U. Keller, Optica **2**, 405 (2015).
[30]P. Kruit and F. H. Read, J. Phys. E: Sci. Instrum. **16**, 313 (1983).
[31]M. Fiess, M. Schultze, E. Goulielmakis, B. Dennhardt, J. Gagnon, M. Hofstetter, R. Kienberger, and F. Krausz, Rev. Sci. Instrum. **81**, 093103 (2010).
[32]M. Huppert, I. Jordan, and H. J. Wörner, Rev. Sci. Instrum. **86**, 123106 (2015).
[33]R. Locher, M. Lucchini, J. Herrmann, M. Sabbar, M. Weger, A. Ludwig, L. Castiglioni, M. Greif, M. Hengsberger, L. Gallmann *et al.*, Rev. Sci. Instrum. **85**, 013113 (2014).
[34]M. Schultze, E. Goulielmakis, M. Uiberacker, M. Hofstetter, J. Kim, D. Kim, F. Krausz, and U. Kleineberg, New J. Phys. **9**, 243 (2007).
[35]M. A. Brown, A. Beloqui Redondo, I. Jordan, N. Duyckaerts, M.-T. Lee, M. Ammann, F. Nolting, A. Kleibert, T. Huthwelker, J.-P. Mächler *et al.*, Rev. Sci. Instrum. **84**, 073904 (2013).
[36]N. B. Delone and M. V. Fedorov, Prog. Quantum Electron. **13**, 267 (1989).
[37]J. H. Eberly, J. Javanainen, and K. Rzewski, Phys. Rep. **204**, 331 (1991).
[38]M. Ferray, A. L'Huillier, X. F. Li, L. A. Lompre, G. Mainfray, and C. Manus, J. Phys. B: At., Mol. Opt. Phys. **21**, L31 (1988).
[39]X. F. Li, A. L'Huillier, M. Ferray, L. A. Lompre, and G. Mainfray, Phys. Rev. A **39**, 5751 (1989).
[40]See http://physics.nist.gov/PhysRefData/ASD/levels_form.html for NIST, Nist atomic spectra database.
[41]H. G. Muller, H. B. van Linden van den Heuvell, P. Agostini, G. Petite, A. Antonetti, M. Franco, and A. Migus, Phys. Rev. Lett. **60**, 565 (1988).
[42]N. Kurahashi, S. Karashima, Y. Tang, T. Horio, B. Abulimiti, Y.-I. Suzuki, Y. Ogi, M. Oura, and T. Suzuki, J. Chem. Phys. **140**, 174506 (2014).
[43]G. Olivieri, A. Goel, A. Kleibert, D. Cvetko, and M. A. Brown, Phys. Chem. Chem. Phys. **18**, 29506 (2016).
[44]N. Preissler, F. Buchner, T. Schultz, and A. Lübcke, J. Phys. Chem. B **117**, 2422 (2013).
[45]M. S. Banna, B. H. McQuaide, R. Malutzki, and V. Schmidt, J. Chem. Phys. **84**, 4739 (1986).
[46]B. Winter, R. Weber, W. Widdra, M. Dittmar, M. Faubel, and I. V. Hertel, J. Phys. Chem. A **108**, 2625 (2004).